First evidence that emerging pinnatoxin-G, a contaminant of shellfish, reaches the brain and crosses the placental barrier

Denis Servent, Carole Malgorn, Mylène Bernes, Sophie Gil, Christelle Simasotchi, Anne-Sophie Hérard, Thierry Delzescaux, Robert Thai, Peggy Barbe, Mathilde Keck, et al.

First evidence that emerging pinnatoxin-G, a contaminant of shellfish, reaches the brain and crosses the placental barrier

Denis Servent[a*], Carole Malgorn[a], Mylène Bernes[a], Sophie Gil[b], Christelle Simasotchi[b], Anne-Sophie Hérard[c], Thierry Delzescaux[c], Robert Thai[a], Peggy Barbe[a], Mathilde Keck[a], Fabrice Beau[a], Armen Zakarian[d], Vincent Dive[a], Jordi Molgó[a*]

[a] Université Paris-Saclay, CEA, INRAE, Département Médicaments et Technologies pour la Santé (DMTS), SIMoS, ERL CNRS 9004, F-91191 Gif sur Yvette, France.

[b] Université de Paris, UMR-S1139, Faculté de Pharmacie de Paris, France.

[c] Université Paris-Saclay, UMR9199, CNRS, CEA, MIRCen, Fontenay-aux-Roses, France.

[d] University of California, Santa Barbara, Department of Chemistry and Biochemistry, CA, 93106-9510, U.S.A.

* Corresponding authors:

Denis Servent & Jordi Molgó. Université Paris-Saclay, CEA, INRAE, Département Médicaments et Technologies pour la Santé (DMTS), SIMoS, ERL CNRS 9004, F-91191 Gif sur Yvette, France

denis.servent@cea.fr (orcid.org/0000-0002-0774-1691); jordi.molgo@cea.fr (orcid.org/0000-0002-0693-8994)

First evidence that emerging pinnatoxin-G, a contaminant of shellfish, reaches the brain and crosses the placental barrier

Denis Servent[a*], Carole Malgorn[a], Mylène Bernes[a], Sophie Gil[b], Christelle Simasotchi[b], Anne-Sophie Hérard[c], Thierry Delzescaux[c], Robert Thai[a], Peggy Barbe[a], Mathilde Keck[a], Fabrice Beau[a], Armen Zakarian[d], Vincent Dive[a], Jordi Molgó[a*]

[a] Université Paris-Saclay, CEA, INRAE, Département Médicaments et Technologies pour la Santé (DMTS), SIMoS, ERL CNRS 9004, F-91191 Gif sur Yvette, France.

[b] Université de Paris, UMR-S1139, Faculté de Pharmacie de Paris, France.

[c] Université Paris-Saclay, UMR9199, CNRS, CEA, MIRCen, Fontenay-aux-Roses, France.

[d] University of California, Santa Barbara, Department of Chemistry and Biochemistry, CA, 93106-9510, U.S.A.

* Corresponding authors:

Denis Servent & Jordi Molgó. Université Paris-Saclay, CEA, INRAE, Département Médicaments et Technologies pour la Santé (DMTS), SIMoS, ERL CNRS 9004, F-91191 Gif sur Yvette, France

denis.servent@cea.fr (orcid.org/0000-0002-0774-1691); jordi.molgo@cea.fr (orcid.org/0000-0002-0693-8994)

ABSTRACT

Massive proliferation of some toxic marine dinoflagellates is responsible for the occurrence of harmful algal blooms and the contamination of fish and shellfish worldwide. Pinnatoxins (PnTx) (A-H) comprise an emerging phycotoxin family belonging to the cyclic imine toxin group. Interest has been focused on these lipophilic, fast-acting and highly potent toxins because they are widely found in contaminated shellfish, and can represent a risk for seafood consumers. PnTx display a potent antagonist effect on nicotinic acetylcholine receptors (nAChR), and in this study we assessed *in vivo* the ability of PnTx-G to cross physiological barriers to reach its molecular target. Radiolabeled [^{3}H]-PnTx-G synthesized with good radiochemical purity and yield retained the high affinity of the natural toxin. Oral gavage or intravenous administration to adult rats and digital autoradiographic analyses revealed the biodistribution and toxicokinetics of [^{3}H]-PnTx-G, which is rapidly cleared from blood, and accumulates in the liver and small intestine. The labeling of peripheral and brain adult/embryo rat tissues highlights its ability to cross the intestinal, blood-brain and placental barriers. High-resolution 3D-imaging and *in vitro* competition studies on rat embryo sections revealed the specificity of [^{3}H]-PnTx-G binding and its selectivity for muscle and neuronal nAChR subtypes (such as α7 subtype). The use of a human perfused cotyledon model and mass spectrometry analyses disclosed that PnTx-G crosses the human placental barrier. The increasing worldwide occurrence of both the dinoflagellate *Vulcanodinium rugosum* and PnTx-contaminated shellfish, due to climate warming, raises concerns about the potential adverse impact that exposure to pinnatoxins may have for human health.

Keywords: Pinnatoxins; Cyclic imine toxins; Nicotinic acetylcholine receptors; Harmful algal bloom; Toxicokinetics; Digital autoradiography

Abbreviations: CI, cyclic imine; PnTx, pinnatoxins; nAChR, nicotinic acetylcholine receptor; MS, mass spectrometry; FTR, fetal transfer rate; MLA, methyllycaconitine; SUG, superficial gray layer of the superior colliculus

1. Introduction

Cyclic imine (CI) toxins produced by various species of marine dinoflagellates constitute a widely distributed group of phycotoxins, comprising the prorocentrolides, spiro-prorocentrimine, gymnodimines, spirolides, pinnatoxins, pteriatoxins, and portimines, with increasing prevalence in the global environment (Molgó et al., 2017; Stivala et al., 2015). The warming of ocean temperatures and increases in nutrients have driven an intensification of harmful algal bloom events (Anderson et al., 2012; Farabegoli et al., 2018; Griffith and Gobler, 2020; Hallegraeff, 2010; Van Dolah, 2000). During these active dinoflagellate blooms, phycotoxins can accumulate in shellfish tissues and be transferred into crabs, fish, seabirds, marine mammals and ultimately to humans (Molgó et al., 2014).

In recent years, there is increasing evidence for the occurrence of emerging pinnatoxins (PnTx) in various wild or commercial shellfish species, collected at different periods of the year, and in different marine waters. Among the eight known PnTxs (A to H), PnTx-G is the most commonly found contaminating shellfish in European waters (Aráoz et al., 2020; Kvrgić et al., 2021; McCarthy et al., 2015; Moreiras et al., 2019; Otero et al., 2019; Otero et al., 2020; Rambla-Alegre et al., 2018; Varriale et al., 2021). In addition, PnTx-G, as well as PnTx-E and PnTx-F, have been detected in Japan, Australia, New Zealand and Canada (reviewed in (Molgó et al., 2014)), and in commercial mussels from Chile (Otero et al., 2020). The cosmopolitan dinoflagellate *Vulcanodinium rugosum* is the producer of PnTx-G (Nézan and Chomérat, 2011; Rhodes et al., 2011), and its growth rate and PnTx-G production are reported to be highest at temperatures ranging between 25 and 30°C (Abadie et al., 2016). PnTx-G levels in contaminated mussels at the Mediterranean Ingril lagoon (France) ranged between 261 and 1,244 µg/kg (Anses, 2019; Hess et al., 2013), values that are much higher than those reported in contaminated shellfish from other locations: 115 µg/kg in Norway (Rundberget et al., 2011), 59 µg/kg in Spain (Garcia-Altares et al., 2014) and 83 µg/kg in Canada (McCarron et al., 2012). In 2019, the French Agency for Food, Environmental and Occupational Health and Safety (Anses, 2019; Arnich et al., 2020), established a detailed view regarding the occurrence of PnTxs in shellfish, establishing a contamination value of 23 µg PnTx-G/kg of total meat not to be exceeded.

Consequently, a risk for human consumers may exist (Arnich et al., 2020; Delcourt et al., 2019) when PnTx shellfish accumulation reaches higher levels.

PnTx were identified as potent antagonists of embryonic and mature muscle ($\alpha1_2\beta\gamma\delta$ and $\alpha1_2\beta\varepsilon\delta$), and neuronal ($\alpha7$, $\alpha3\beta2$, $\alpha4\beta2$) nicotinic acetylcholine receptor (nAChR) subtypes (Aráoz et al., 2011; Benoit et al., 2019; Hellyer et al., 2015). At the structural level, their seven-membered CI ring fits perfectly with the receptor subunit interface of nAChRs, while the unique substructures of the macrocyclic framework of the PnTx extend radially from the binding pocket to engage in distinctive interactions with the complementary and variable face F of the nAChRs (Bourne et al., 2015). The interaction of PnTx with nAChRs was shown in mice to induce exceptionally rapid lethality associated with central neurological symptoms and flaccid paralysis (Munday et al., 2012; Selwood et al., 2010). In addition, due to their high chemical stability (Jackson et al., 2012; Selwood et al., 2014), PnTx exhibit high oral acute toxicity in mice (Arnich et al., 2020; Delcourt et al., 2019; Munday et al., 2012; Sosa et al., 2020), suggesting that they cross the intestinal barrier.

Interestingly, a recent publication reported that a *V. rugosum* bloom in Cuba induced acute skin irritation in swimmers. The bloom contained CI toxins such as pinnatoxins and portimine, which could have caused dermatitis (Moreira-González et al., 2021). Even though no information has been reported yet linking CI toxins to neurotoxic events in humans, the potent interaction of PnTx with central and peripheral nAChRs raises concerns about the harmful downstream effects of PnTx exposure.

In the present study, we chose to study the ability of PnTx-G to cross physiological barriers, because: (i) it is a chemically stable molecule and is considered as the precursor of other pinnatoxins (A-C) in mollusks, (ii) it is a common shellfish contaminant distributed worldwide, and (iii) it can be chemically synthesized and radiolabeled with tritium allowing its detection using high-resolution digital autoradiographic analyses. As demonstrated herein, the toxicokinetic profile of [^{3}H]-PnTx-G in rats reveals its rapid blood clearance, large tissue distribution, and its ability to cross the intestinal, blood-brain and placental barriers. Finally, using a human perfused placenta cotyledon model and mass spectrometry analysis, the ability of PnTx-G to pass through the human placental barrier is confirmed.

2. Materials and Methods

2.1. Synthesis and spectral analysis of radiolabeled [^{3}H]-PnTx-G

Among the PnTx family, PnTx-G is the only one that has proven amenable to tritium labeling so far by partial hydrogenation reaction (Fig. S1, Supplementary materials). Based on a previously reported total synthesis (Aráoz et al., 2011), the protocol afforded [^{3}H]-PnTx-G with a radiochemical purity greater than 97%, and a specific activity of 40 Ci/mmol.

2.2. Characterization and validation of [^{3}H]-PnTx-G

The α7/5HT$_3$ chimera was transiently transfected into tsA-201 cells using 15 µg cDNA for ca. 10^7 cells per Petri dish. All binding experiments were performed in 96-well GF/C plates pre-soaked in 0.5% polyethylenimine, and using PBS buffer complemented with 0.1% BSA. The reaction was stopped by simultaneous filtration of the 96 wells with a FilterMate harvester (PerkinElmer, France). The filters were washed twice with ice-cold buffer and dried, 25 µl of MicroScint was added, and the bound radioactivity was counted by scintillation spectrometry on a TopCount beta counter (PerkinElmer, France).

Equilibrium competition with the α7/5HT$_3$ chimera used a cell density adjusted to bind specifically no more than 10% of [^{3}H]-PnTx-G (1 nM). IC_{50} values were determined by fitting the competition data with a Hill equation and conversion to K_i constants using the equation: $K_i = IC_{50}/(1+L^*/K_d)$. Association kinetic experiments were performed with 3 different concentrations of [^{3}H]-PnTx-G (1, 1.9 and 3.6 nM) and the apparent association constants obtained from these experiments were plotted against the tracer concentrations. The slope of this line corresponds to the association kinetic constant Kon. Dissociation experiments were performed at 1.9 nM of [^{3}H]-PnTx-G and the dissociation was measured for 3 h after the addition of 1 µM of PnTx-G. Each experiment was performed two times in duplicate.

2.3. In vivo experiments

129 2.3.1 Ethical compliance

130 Animal care and surgical procedures were performed according to the Directive 2010/63/EU of the
131 European Parliament, which had been approved by the Ministry of Agriculture, France. The project
132 was submitted to the French Ethics Committee CEEA (Comité d'Ethique en Expérimentation
133 Animale) and obtained the authorization APAFIS#4111-2016021613253432 v5. All experiments were
134 performed in accordance with relevant named guidelines and regulations. Experiments were conducted
135 on adult Wistar rats from Janvier Labs (Le Genest St Isle, France).

136

137 2.3.2 Toxicokinetics, organ distribution, and elimination

138 Wistar male rats were anesthetized with 2% isoflurane (Iso-vet®, Piramal, UK). A 22G Surflo i.v.
139 catheter (Terumo, Japan) was inserted into the tail vein for intravenous (i.v.) injection of [^{3}H]-PnTx-G
140 at 3 µg/kg. This dose was selected because was not lethal to rats, as determined by a 24 h period of
141 observation. Blood samples were collected between 2 and 15 min after i.v. injection. Animals were
142 euthanized 15 min after [^{3}H]-PnTx-G administration, and perfused with 0.9% NaCl (30 mL/rat, 300
143 mL/h) for collection of major organs. Urine and feces were collected 4 h after administration.
144 Quantification of β-radioactivity contained in blood and organs was performed using a Liquid
145 Scintillation Analyzer (Tri-Carb 2100TR, Packard BioScience Company, USA). Toxicokinetic
146 parameters were calculated with the non-compartmental analysis Linear up/Log down method, using
147 the PKSolver add-in program (Excel).

148 2.3.3 Investigation of biological barriers crossing

149 Fasted rats were exposed by oral gavage to 100 µg/kg of [^{3}H]-PnTx-G in PBS. The dose was
150 chosen on the basis of our own preliminary studies, given that it is not lethal to rats, and because it
151 corresponds to about 4 times the proposed maximum tolerable concentration of PnTX-G
152 contaminating shellfish (23 µg PnTX G/kg of total meat) (see Introduction). We used oral gavage,
153 instead of intraperitoneal administration, since the oral route of administration is the one that may be
154 related to consumption of contaminated shellfish in humans, and because it assures less variability,
155 pain, and discomfort for the animals. The administration by gavage followed the OECD

156 recommendations for the testing of chemicals. Rats were euthanized 6 h after exposure to the
157 radiolabeled toxin.

158 Tissue sections were prepared on a microtome and analyzed by digital autoradiography.

159 Pregnant female rats were i.v. injected 19 days after fertilization with 10 µg/kg of [^{3}H]-PnTx-G to
160 explore the ability of PnTx-G to cross the placental barrier. The dose was chosen for the reason that is
161 not lethal to pregnant rats, according to our preliminary studies. Rats were euthanized 30 min later and
162 perfused with 0.9% NaCl. Embryos and placentas were rapidly collected and snap-frozen to prepare
163 whole-body sagittal tissue sections, for digital autoradiographic analyses and to measure radioactivity
164 content.

165

166 *2.4. Digital autoradiography*

167 The analyzed organs were maintained in mounting medium, and tissue sections (20 µm thick) were
168 cut at −20 °C with a slicing microtome (Leica Microsystems, France). The microtome was carefully
169 cleaned with water-ethanol solution between treatment of each sample to remove any trace of
170 radioactivity and avoid contamination between different organs. The absence of radioactive
171 contaminants in the rinsing solution was checked by radioimaging of drop samples. The tissue sections
172 were placed on glass slides and were either stored in a freezer for microscopy analyses or kept at room
173 temperature for 1 day in the presence of silica gel to ensure complete drying for proper radioimaging.
174 A high-performance autoradiography imager (β-imager 2000, Biospace Lab, Paris, France) allowing
175 real-time radioactive imaging through direct β-particle counting and absolute radioactivity
176 quantification (detection threshold of 0.001 cpm/mm^2 for ^{3}H) was used to measure radioactivity in
177 dried tissue sections. These sections were analyzed by radioimaging at high resolution and sensitivity
178 (125 µm resolution and 0.5 pCi detection threshold) using digital autoradiography, to determine the
179 count/per tissue section volume, which was converted to total radioactivity per organ on the basis of
180 the total volume of each organ (determined by organ weighing)

181 The time of acquisition on the β-Imager was 1 h for peripheral organ preparations and 24 h for
182 brain sections.

183 *2.5. HPLC analysis of organ extracts*

184 Soluble extracts of spleen, liver and whole brain from rats sacrificed 30 min post-injection were
185 prepared as follows: organs were resuspended in 3 mL TFA (trifluoroacetic acid) and homogenized
186 using an Ultra Turrax® system (IKA-Werke, Gmbh & Co Kg, Staufen, Germany). The homogenate
187 was rinsed with 15 mL of MilliQ H_2O and was kept on ice for 5 min before being centrifuged (8,000
188 rpm, 15 min at 4°C). Supernatants were collected, analyzed with radio-HPLC (Kromasyl HPLC C18
189 column 4.6 x 150 mm) and compared to control analysis of [^{3}H]-PnTx-G.
190
191 *2.6. Reconstruction 3D images*

192 Six embryos from 2 pregnant rats were recovered for histological and autoradiographic analyses.
193 After euthanasia, embryos were immediately frozen at -40 °C in isopentane. They were cut into 20-µm
194 thick sections (sagittal embryo sections, coronal brain sections) with a CM3050S cryostat (Leica,
195 Rueil-Malmaison, France). Every fourth section was mounted on Superfrost glass slides, and rapidly
196 dried in a desiccator. After autoradiography imaging, the same sections were processed for Nissl
197 staining, to obtain additional information about brain anatomy. Images from the embryo surface,
198 corresponding to sections subsequently processed, were recorded before sectioning using a digital
199 camera (Oscar F-810C, 8 megapixels, Allied Vision Technologies, Stadtroda, Germany) with an in-
200 plane resolution of 27 × 27 µm^2. Block-face photographs were stacked and tissue was automatically
201 segmented using a histogram analysis method. As these images were taken prior to sectioning at the
202 exact same position section after section when the imaged tissue was still attached to the block, so the
203 resulting stack of photographs was therefore intrinsically 3D spatially coherent.

204 To further refine the toxin biodistribution in the rat embryo, we applied a protocol previously
205 developed to obtain 3D imaging of adult animal brain from tissue sections (Dauguet et al., 2007). As
206 shown in supplementary material (Fig. S3, Supplementary information) 66 sagittal embryo section
207 images were produced consecutively by photography, histological coloration (cresyl violet) and digital
208 autoradiography, allowing 3D reconstruction of the volumes by co-alignment of the block face,
209 histological and autoradiographic slices. The digitalization of the autoradiography and histological

sections and the 3D reconstruction of the images are described in detail in the supplementary materials.

2.7. Passage through the human placental barrier

2.7.1 Mass calibration and analysis

The mass spectrometry analysis of PnTx-G was described in supplementary materials section.

2.7.2 Human placental perfused cotyledon model

Term placentas (37-40 weeks of gestation) from uneventful pregnancies were immediately collected after vaginal delivery or cesarean section from the Port-Royal Hospital Obstetrics Department (Paris, France). The enrolled patients did not receive any medication, except for epidural analgesia or oxytocin during labor, and did not present any vascular disease such as diabetes mellitus, preeclampsia, or intra-uterine growth restriction. These placentas were obtained following informed patient written consent and approval from our local ethics committee (CPP Paris Ile-de-France 3, N-18-05, Paris, France). Collected placentas (n = 3) were perfused in a double circuit according to a validated method as previously described (Ceccaldi et al., 2009). Maternal and fetal solutions were prepared with Earle's medium containing 25 g/L bovine serum albumin (Euromedex, Souffelweyersheim, France). The pH of the maternal and fetal compartments was adjusted to 7.4 ± 0.1 and 7.2 ± 0.1, respectively.

Perfusion experiments were started within 20 min after delivery. After a visual examination to confirm the vascular integrity of both maternal and fetal sides, a distal branch of a fetal artery and its associated vein that were supplying a selected cotyledon were cannulated. The fetal circulation was established at a flow rate of 6 $mL.min^{-1}$ (to ensure a balance between arterial and fetal venous flow). Placentas with evidence of vascular leakage were discarded. On the maternal side, the perfused area progressively whitened, which allowed visualization of the chosen cotyledon. After a wash step of 10 min, the maternal perfusion was initiated by inserting two catheters into the intervillous space on the maternal side. The maternal circulation was established at a flow rate of 12 $mL.min^{-1}$. Parameters such as perfusion pressure in the fetal vasculature and potential fluid leakage from the fetal circulation were

monitored to check the technical process. After an additional wash step of 5 min, a freely diffusing marker, antipyrine, was added to the maternal medium (final concentration 20 mg/L) and PnTx-G (100 nM) was subsequently added to the same compartment. The perfusion duration was 90 min with maternal recirculation. Samples from the maternal circulation and venous fetal circulation were collected at 0, 15, 30, 45, 60, 75 and 90 min, in order to monitor toxin concentrations. At the end of perfusion, all the samples were stored at -80°C until toxin analysis. Standard parameters were calculated according to Challier's formulas (Challier, 1985). Placental transfer was estimated from two transport parameters: the fetal transfer rate (FTR) and the clearance index. Calculating the clearance index allowed comparison of results during different experiments and evaluation of the index of trans-placental transfer from one placental unit to another.

The two transport parameters were calculated as follows:

- The Fetal Transfer Rate (FTR) = (Cf / Cm) x 100, where Cf is the venous fetal concentration of a molecule and Cm is the maternal concentration of the same molecule. The result is given as a percentage. FTR for antipyrine had to be over 20% as described by Challier (Challier, 1985).
- The Clearance Index = FTR (pinnatoxin)/FTR (antiypirine).

2.8. In vitro competition experiments

Adult rats or rat embryos were euthanized and the whole embryos (n = 3) or adult brains (n = 3) were immediately frozen at -80°C. In turn, 16 and 42 coronal sections (20 µm) of embryo and brain from each rat were cut and mounted onto chrome/gelatin coated slides and allowed to air dry overnight before being frozen again. All sections were preincubated in KRH buffer (20 mM HEPES, 118 mM NaCl, 4.8 mM KCl, 2.5 mM $CaCl_2$ and 1.2 mM $MgSO_4$) at 4°C for 30 min. Then, all sections were incubated in cold KRH buffer for 90 min with 0.3 nM [^{3}H]-PnTx-G with or without the different competitors (cold 0.3 µM PnTx-G, 0.25 µM αC-conotoxin PrXA, 100 nM MLA for embryo slices and 0.3 µM PnTx-G, 100 nM MLA (methyllycaconitine) or 5 nM A-85380 for brain preparations). The sections were rinsed twice in cold KRH buffer then twice in cold 20 mM HEPES buffer, and finally

rinsed in distilled water. As previously described, these sections were analyzed by digital autoradiography for 24 h (embryo sections) or 64 h (brain sections).

2.9. Statistics and Reproducibility

All quantitative measures were performed as independent replicates. All attempts to replicate the data were consistent. Statistical analyses and sample sizes are described in the pertinent figure legends. Statistical analysis was performed using Prism 7 software (GraphPad Software, San Diego, CA, USA). Differences between values were tested using the unpaired Student's *t*-test, and samples were considered statistically significant when $P < 0.05$.

3. Results

3.1. Binding properties of *[^{3}H]-PnTx-G*

In vitro and *in vivo* properties of PnTx-G were evaluated using its tritium labeled form ([^{3}H]-PnTx-G), a labeling that fully preserves toxin bioactivity. The pharmacological properties of [^{3}H]-PnTx-G were evaluated by kinetic binding experiments on the α7 receptor subtype (α7-5HT$_3$ chimeric receptor) in order to measure its association and dissociation rate constants. These values, were respectively 7.7 10^5 $M^{-1}.sec^{-1}$ and 1.7 10^{-4} sec^{-1} (Fig. S2a, S2b, Supplementary information), leading to a dissociation constant (Kd = 0.22 nM), similar in value to that determined by competition binding experiments, or in previously described results using [^{125}I]-α-bungarotoxin ([^{125}I]-α-BgTx) as radiotracer (Fig. S2c, Table S1, Supplementary information).

3.2. In vivo toxicokinetics, organ distribution and elimination of [^{3}H]-PnTx-G

Maximum blood β-radioactivity concentration of [^{3}H]-PnTx-G was observed 2 min after i.v. administration (T_{max}), representing 16.3 ± 3.2% of the administered dose (Fig. 1). The blood β-radioactivity concentration of [^{3}H]-PnTx-G decreased after T_{max}, showing a value of 6.9 ± 0.4% of the administered dose 15 min after administration (Fig. 1a). The kinetic profile of [^{3}H]-PnTx-G presented

an exponential decrease in radioactivity with a final elimination characterized by a terminal half-life, $T_{1/2}$, equal to 13 ± 4 min and an elimination constant equal to 0.06 ± 0.02 min^{-1}. The estimated AUC_{0-t} was 5.24 ± 0.76 min.µCi/mL. The distribution volume was 117.4 ± 34.4 mL and the clearance 6.3 ± 0.1 mL/min (Table 1). Maximum organ radioactivity concentrations of [^{3}H]-PnTx-G were observed in the liver and small intestine 15 min after administration, with 14.6 ± 4.4% and 17.5 ± 6.0% of the administered dose, respectively (Fig. 1b). Urine elimination represented 3.6 ± 0.6% of the administered dose, 15 min after injection, whereas feces elimination after 4 h accounted for only 0.04 ± 0.02% of the administered dose (Fig. 1b).

3.3 PnTx-G crosses the intestinal and blood-brain barriers of adult rats

Previous studies have reported acute toxicity of PnTx-G in mice through respiratory failure after oral administration (Arnich et al., 2020; Munday et al., 2012; Sosa et al., 2020), suggesting the capacity of this toxin to cross the intestinal barrier.

As shown in Fig. 2a, when [^{3}H]-PnTx-G was administered orally to rats the radioactivity was observed in peripheral organs such as liver, kidney and spleen, but also in various brain regions such as the hippocampus and superficial gray layer of the superior colliculus (SuG). Interestingly, the biodistribution of the toxin 15 min after i.v. injection in the brain was similar to that observed after oral gavage. Further systematic tissue analyses revealed the presence of radioactivity in skeletal muscles such as the *extensor digitorum longus* (EDL) and gastrocnemius muscles (Fig. 2b). In these muscles, the particular labeling of the radioactivity signal followed the distribution of the $\alpha1_2\beta1\varepsilon\delta$ muscle-type nAChR at skeletal neuromuscular junctions, an observation in agreement with the interaction of PnTx-G with this receptor subtype. Similarly, the presence of radioactivity in the hippocampus, SuG and hypothalamus would correspond to the toxin binding to various neuronal nAChR subtypes known to be expressed in these brain structures.

Soluble extracts of spleen, whole brain and liver from rats euthanized 30 min post-injection were prepared and analyzed by HPLC coupled to a radioactivity detector. For the spleen, a single radioactivity peak eluting at the retention time of the native standard toxin was observed,

demonstrating the stability of pinnatoxin during its distribution phases in this organ (Fig. 3a). In brain extracts, in addition to the major native PnTx-G peak, minor metabolite peaks were also detected, corresponding to 20% of the injected toxin. This percentage rose to 45% in liver extracts (Fig. 3a), indicating a possible role of this organ in PnTx-G metabolization.

3.4 PnTx-G crosses the placental barrier

The ability of PnTx-G to cross the placental barrier was evaluated by injecting i.v. [^{3}H]-PnTx-G to pregnant rats (19 days after fertilization) and determining the presence of the radiolabeled toxin in the placenta and in embryos. Thirty minutes after the [^{3}H]-PnTx-G injection, the mean radioactivity present in placentas corresponded to 0.73 % of the injected dose, while in embryos represented 0.45 %.

As shown by the whole-body sagittal autoradiographic sections in Fig. 4a, different rat embryo tissues were labeled by the [^{3}H]-PnTx-G, including the tongue, limb skeletal muscles, the spinal cord and various brain regions, demonstrating the toxin's ability to cross the placental barrier and to distribute into various tissues/organs. This labeling was highly reproducible in different sections from three different embryos (Fig. 4a), and the radioactivity was associated with the intact toxin, as revealed by radio-HPLC analyses of whole embryo extracts (Fig. 3b) (Dauguet et al., 2007). To further refine the [^{3}H]-PnTx-G toxin biodistribution in the rat embryo, 3D reconstruction imaging was performed. As can be seen in Fig. 4b, the toxin labels several peripheral organs such as the tongue, the liver, the hindlimb and forelimb skeletal muscles, and several areas of the central nervous system, such as the medulla oblongata, the pons, the trigeminal nerve and the cervical and thoracic ganglia.

The capacity of PnTx-G to cross the placental barrier was studied further, using a human perfused *ex vivo* cotyledon model, and quantitative detection of the intact toxin in maternal and fetal compartments (Fig. 5d) by mass spectrometry. For this, a mass spectrometry analysis of the PnTx-G standard was first performed (Fig. 5a), followed by the construction of a calibration curve for PnTx-G spiked at different known concentrations in naïve human placental perfusates (Fig. 5b) and submitted to an extraction protocol before analysis by MALDI-TOF spectrometry. The PnTx-G concentrations

detected in the maternal and fetal compartments, as a function of time (0-90 min), are shown in Fig. 5c, and the results of three placentas that were sucessfully perfused and validated using the mean fetal transfer rate (FTR) of antipyrine are shown in Fig. 5e. These studies showed that a maximum value of FTR was reached after 15 min of perfusion, and decreased slightly due to maternal recirculation (Fig. 5d-e). In comparison, the kinetics of the PnTx-G clearance index during the perfusion procedure increased up to 30 min, and then reached a plateau up to 90 min (Fig. 5e). The mean clearance index of PnTx-G was 1.65 ± 0.17, indicating that the FTR of the toxin is higher than the FTR of antipyrine, which undergoes only passive diffusion and is used to measure tissue integrity/membrane permeability.

Since antipyrine neither binds to proteins nor accumulates in placental tissue, its transfer rate depends only on fetal and maternal flows, which should be constant during the perfusion. Hence, a clearance index value close to 1 demonstrates a mechanism of placental transfer by passive diffusion without placental accumulation (Challier, 1985). In this case, PnTx-G transfer was significantly higher than the transfer rate of antipyrine, reaching a value close to 2, indicating a rapid significant facilitated transfer of the toxin ($p = 0.032$).

3.5 The nAChR receptor subtypes targeted by PnTx-G in rat embryos and adult rats

In an attempt to identify the main nAChR subtypes targeted by PnTx-G in rat embryos, whole-body sagittal sections of rat embryos were prepared and incubated with [^{3}H]-PnTx-G (0.3 nM) alone, or in the presence of three competitive ligands known to interact with different nAChR subtypes with various selectivity profiles (Table S2, Supplementary information). Digital autoradiographic analyses of these embryo sections (Fig. 6) highlighted first that the [^{3}H]-PnTx-G labeling obtained in this *in vitro* experiment is impressively similar to that previously observed after *in vivo* toxin exposure (see Fig. 4). This observation validates the use of *in vitro* labeling to study the binding specificity of the toxin *in vivo*. Secondly, unlabeled PnTx-G (0.3 µM) largely displaced (up to 90%) [^{3}H]-PnTx-G binding, emphasizing the specificity of the toxin labeling in these tissues (Fig. 6a). Interestingly, αC-conotoxin PrXA (0.25 µM), a ligand known to selectively interact with muscle-type nAChR (El-Aziz et al., 2017; Jimenez et al., 2007), induced a large decrease of the labeling, highlighting the crucial role

of this receptor subtype in the toxin interaction. This was particularly obvious in peripheral organs such as the tongue or forelimb skeletal muscles, while the spinal cord and brain regions remained largely labeled. In contrast, MLA (100 nM), a specific α7 antagonist (Ward et al., 1990), displaced [^{3}H]-PnTx-G labeling only weakly, but more efficiently in the CNS, such as the pineal gland and spinal cord regions (Fig. 6a). These observations suggest that $\alpha1_2\beta1\gamma\delta$ and α7 nAChRs are important targets for the toxin, in good agreement with the high affinity of PnTx for these two receptor subtypes (Table S2, Supplementary information), and with previous embryo labeling.

Furthermore, to assess the specificity of [^{3}H]-PnTx-G binding to nAChR subtypes in various adult rat brain regions, *in vitro* competition experiments were performed on brain tissue sections in the absence or presence of various specific antagonists of nAChR subtypes: unlabeled PnTx-G, the selective α7 nAChR antagonist MLA, and A-85380, a selective binder of the α4β2 receptor subtype (Sullivan et al., 1996) (Table S2, Supplementary information). Here again, it is worth mentioning that *in vitro* brain imaging reproduced what was observed after *in vivo* exposure, suggesting, along with competition experiments (see below), that the labeling is due to intact PnTx-G. Non-radioactive PnTx-G completely abrogates the labeling of the radioactive toxin, demonstrating the specificity of this interaction in the central nervous system (Fig. 6b). Using MLA, a large part of the [^{3}H]-PnTx-G labeling was abolished, especially in hippocampus and hypothalamus regions, revealing a selective toxin-α7 receptor interaction in these regions, as well as the high content of this receptor subtype in these brain areas (Fig. 6b). In the SuG region, MLA was less efficient than A-85380 in decreasing the [^{3}H]-PnTx-G-associated radioactivity, suggesting the prevalence of β2-selective nAChRs in this area, and in particular the α4β2 subtype, as previously reported (Baddick and Marks, 2011; Marks et al., 2011). In contrast, A-85380 was inefficient in abolishing the labeling in hippocampus and hypothalamus regions (Fig. 6b). These results highlight the prevalence of [^{3}H]-PnTx-G labeling for α7 nAChR in brain, even if other subtypes, such as the α4β2 subtype, also seem to be recognized, but to a lesser extent.

4. Discussion

PnTx belong to the CI toxin family, an emerging class of more than 40 different marine toxins produced by dinoflagellates and distributed worldwide. Interestingly, among all the CI toxins, PnTx display severe toxic effects after oral administration to mice, associated with piloerection, prostration, decreased mobility (occasionally preceded by an initial phase of hyperactivity immediately following administration), hypothermia, hind leg paralysis, abdominal breathing and cyanosis, and finally death by respiratory arrest (Arnich et al., 2020; Delcourt et al., 2019; Munday et al., 2012; Sosa et al., 2020). These neurotoxic properties have been correlated with their high potency to block various central and peripheral nAChR subtypes (Aráoz et al., 2011; Delcourt et al., 2019; Molgó et al., 2017). Nevertheless, no human poisoning has yet been associated with their ingestion via contaminated shellfish. This may be because recent monitoring shows that reported PnTx-G levels are below the threshold value proposed by Anses (2019) of 23 µg/kg of total meat for contaminated shellfish in various European shellfish production areas (Kvrgić et al., 2021; Lamas et al., 2019; Moreiras et al., 2019; Otero et al., 2019; Otero et al., 2020; Rambla-Alegre et al., 2018; Varriale et al., 2021). On the other hand, in places where PnTx-G levels were high, as in the Mediterranean Ingril lagoon (Anses, 2019; Aráoz et al., 2020; Hess et al., 2013), wild shellfish collection has been banned (since January 1, 2020) by the health authorities because of the possible health risk to shellfish consumers. Interestingly, a recent publication suggests a possible link between PnTx and portimine release during a *V. rugosum* bloom and acute dermal irritation in sixty people (mostly children) who had prolonged contact with the dinoflagellate bloom in Cuba's Caribbean waters (Moreira-González et al., 2021).

In the present study, we addressed more precisely the toxicokinetic properties of PnTx-G, how PnTx interact *in vivo* with their central and peripheral receptor targets, and how easily they cross physiological barriers. First, the rapid blood clearance of [^{3}H]-PnTx-G ($t_{1/2}$ = 13 min) was shown, as well as its distribution in several peripheral organs and in the brain. In addition, using digital autoradiographic approaches in the adult rat, we provide evidence that after oral gavage or i.v. injection, [^{3}H]-PnTx-G crosses the intestinal and blood-brain barriers to target skeletal muscle and brain neuronal nAChR subtypes, respectively. Despite possible minor metabolization of PnTx-G in the brain, the labeling of the main brain structures by the intact toxin was supported by autoradiographic competition experiments performed on brain tissue sections. Indeed, to determine the subtypes of

neuronal nAChRs involved, coronal rat brain sections were incubated with [^{3}H]-PnTx-G alone, or in the presence of selective nAChR ligands, highlighting the major target role of the α7 nAChR subtype in the central nervous system. The ability of CI toxins to cross the blood-brain barrier was first suggested by transcriptional and immunohistochemical analysis showing that neuronal nAChRs were upregulated after intraperitoneal spirolide administration to rats (Gill et al., 2003). More recently, mass spectrometry analyses revealed the ability of 13-desmethyl spirolide C to cross the blood-brain barrier in a transgenic mouse model (Alonso et al., 2013), but without any precise information on the brain areas and nAChR subtypes recognized in the central nervous system. Interestingly, the role of α7 nAChR in receptor-mediated transcytosis across the blood-brain barrier was already suggested, and exploited for brain-targeted drug delivery (Huey et al., 2017; Wei et al., 2015). This process could explain the ability of PnTx-G to cross so efficiently the blood-brain barrier, and eventually the other physiological barriers.

Second, biodistribution analyses on full embryo sections after i.v. administration of [^{3}H]-PnTx-G to pregnant rats, associated with 3D reconstruction imaging, revealed the ability of the toxin to cross the placental barrier and to distribute into various peripheral and central organs of the embryos. Intriguingly, the embryonic brain stem regions labeled by the toxin (spinal cord, medulla oblongata, pons) are not similar to those highlighted in the adult rat (hippocampus, SuG, hypothalamus). This observation seems to be in line with the timing of our observation (E19) and the timeline of brain regional neurogenesis in rat in which the spinal cord, medulla and pons mature early (from gestational days 11 to 16), while hippocampus neurogenesis starts later and continues until postnatal days 16-19 (Rice and Barone, 2000). Furthermore, the embryo regions labeled by the toxin superimposed nicely with those described in the eMouse Atlas, which are known to over-express the α7- and α1-nAChRs genes in central and peripheral regions of the mouse embryo (Armit et al., 2017). In line with the ability of PnTx-G to cross the placental barrier in the rat, similar results were established using a human placental perfused cotyledon model. A facilitated transfer of the toxin was observed in this human placental model, suggesting a possible role of nAChRs in this process. This hypothesis seems to reinforce the view of the reported expression of various nAChR subtypes, including α7, in the placenta (Machaalani et al., 2018).

In conclusion, the collective results from this study show that when PnTx-G was ingested, the toxin crossed the intestinal and blood-brain barriers and reached specific brain regions. Our results also demonstrate the placental transport of PnTx-G, following single low-dose exposure of pregnant rats and in a human placental cotyledon model. The significance these outcomes may have for pregnant women exposed to PnTx-G by ingestion of contaminated shellfish is at present unknown. Likewise, the consequences of mammalian fetal exposure to PnTx-G remain to be determined. Nevertheless, a preliminary study tackling the potential developmental toxicity of PnTx in chick embryos has been reported (Couesnon et al., 2014). These results raise many additional questions on the mechanisms by which PnTx target the nervous and impact on the musculoskeletal systems, and on the potential risk associated with long-term consumption of contaminated shellfish on human health.

Figure Legends

Fig. 1. Toxicokinetics, organ distribution and elimination of [^{3}H]-PnTx-G in male rats. (a) Blood PnTx-G β-radioactivity, expressed as a % of the single i.v. dose (3 µg/kg) administered to rats (n=3), as a function of time. Each symbol in the curve represents the mean ± SEM. (b) PnTx-G β-radioactivity in organs, urine and feces, expressed as a % of the administered dose (i.v., 3 µg/kg). Data were determined 15 min (organs and urine) or 4 h (feces) after single i.v. administration to rats (n=3)(mean ± SEM).

Fig. 2 Biodistribution of [^{3}H]-PnTx-G either after oral gavage (100 µg/kg) (a) or i.v. injection (3 µg/kg) (b) of the toxin to rats. Rats were euthanized 6 h (oral gavage, n = 3) or 15 min (iv, n = 3) after exposure to the radiolabeled toxin, and perfused with a solution of NaCl to remove the radioactivity from blood, preceding the radioactivity count of individual organ tissues. The images represent middle sections of peripheral organs and are located at Bregma -5.52 mm in the brain. The intensity scale (blue to red) is proportional to the increase in radioactivity levels (in counts/pixel). The time for image acquisition on the β-Imager was 1 h for peripheral organs and 24 h for the brain. Images are representative of at least 24 sections from 3 rats.

Fig. 3 (a) Radio-HPLC analyses of [^{3}H]-PnTx-G (15 nCi control) and soluble extracts from spleen, brain and liver of rats injected with the toxin. (b) Radio-HPLC analyses of [^{3}H]-PnTx-G (control) and soluble extracts from rat embryo extracts. Soluble extracts of spleen, liver, brain and whole embryos were obtained from rats euthanized 30 min post-i.v. injection, and were prepared using a homogenizer and centrifugation. Supernatants were collected, analyzed with a radio-HPLC column (Kromasyl C18 4.6 x 150 mm), and compared to control analysis of [^{3}H]-PnTx-G.

Fig. 4 Biodistribution of [^{3}H]-PnTx-G in rat embryos, 30 min after i.v. injection of toxin in pregnant rats. (a) Optical (left) and autoradiographic images (right) of rat embryo sagittal sections. Two slices (spaced by 80 µm) representative of the 66 sections from each of the three different embryos were analyzed by digital autoradiography. The intensity scale (blue to red) is proportional to the radioactivity levels (in count/pixel). (b) 3D reconstruction images of [^{3}H]-PnTx-G labeling from 66 embryo sections (see protocols in Methods section) highlighting the regions with the higher or lower radioactivity levels detected using respectively high and low thresholds defined by experts (corresponding respectively to 89% and 83% of the maximal radioactivity value). In blue and green, respective [^{3}H]-PnTx-G labeled regions with α7- and α1-nAChR enriched gene expression(Armit et al., 2017). Tongue in cyan expressed both receptor subtypes and liver and other brain areas are colored in gray.

Fig. 5 Maternal-fetal transfer of PnTx-G in a human perfused *ex vivo* cotyledon model. (a) Mass spectrometry analysis of PnTx-G standard. (b) Calibration curve of PnTx-G that was spiked at different known concentrations in placental perfusates, and submitted to an extraction protocol before analysis by MALDI-TOF spectrometry (mean ± SD, n = 4-6). (c) Measurement in maternal (Perfusate Placenta Maternal (PPM) with maternal recirculation) and fetal (Perfusate Placenta Fetal (PPF) without fetal recirculation) compartments of PnTx-G concentration, from time 0 (T0) to time 90 (T90), in min (mean ± SD, n = 3). (d) Schematic view of the human perfused cotyledon model, and (e) fetal

transfer rate of antipyrine (ATP) and kinetics of clearance index (PnTx-G transfer/antipyrine transfer ratio) of PnTx-G (mean ± SD, n = 3).

Fig. 6 Digital autoradiography of sagittal sections of rat embryos (a) and adult rat coronal brain slices (b) incubated with [^{3}H]-PnTx-G alone or in the presence of selective nAChR ligands. (a) Sagittal sections of rat embryos were prepared and incubated for 90 min with [^{3}H]-PnTx-G (0.3 nM) with or without the different competitors (unlabeled 0.3 µM PnTx-G, 0.25 µM αC-conotoxin PrXA, 100 nM MLA). Each image is representative of one of the 16 slices of each embryo, (n = 3). (b) *In vitro* competition experiments on adult rat coronal brain sections incubated for 90 min with [^{3}H-PnTx-G] and various nAChR antagonist ligand competitors (cold 0.3 µM PnTx-G, 100 nM MLA, 5 nM A-85380). Each image is representative of one of the 42 sections of each brain (bregma B:-6.12) (n = 3). All the sections were analyzed by digital autoradiography after 24 h (embryos sections) or 64 h (brain sections) of acquisition on the β-Imager. The intensity scale (blue to red) is proportional to the increase in radioactivity level (in counts/pixel).

CRediT authorship contribution statement

Denis Servent: Conceptualization, Formal analysis, Funding acquisition, Supervision, Writing - original draft. **Carole Malgorn**: Investigation. **Mylène Bernes**: Investigation. **Sophie Gil**: Investigation, Formal analysis, Writing – review & editing. **Christelle Simasotchi**: Investigation. **Anne-Sophie Hérard**: Investigation, Formal analysis, Writing – review & editing. **Thierry Delzescaux**: Investigation, Formal analysis, Writing – review & editing. **Robert Thai**: Investigation. **Peggy Barbe**: Investigation. **Mathilde Keck**: Investigation, Formal analysis. **Fabrice Beau**: Investigation. **Armen Zakarian**: Investigation, Funding acquisition, Writing – review & editing. **Vincent Dive**: Conceptualization, Formal analysis, Funding acquisition, Supervision, Writing – review & editing. **Jordi Molgó**: Conceptualization, Investigation, Formal analysis, Supervision, Writing – review & editing.

536

537 **Declaration of competing interests**

538 The authors declare that they have no known competing financial interests or personal relationships
539 that could appear to influence the work reported in this paper.

540

541 **Acknowledgements**

542 This work was funded in part by the National Institutes of Health (USA, grants NIGMS R01
543 GM077379, to A.Z, J.M and D.S), by the European Interreg program AlertoxNet (EAPA_317/2016),
544 by the CNRS and the CEA. We thank Mrs Doria Alili and Mrs Patricia Villeneuve for technical
545 assistance.

546

547 **Supplementary Material**

548 Additional supporting information to this article may be found online at:

549

550 ## References

551

552 Abadie E, Muguet A, Berteaux T, Chomerat N, Hess P, Roque D'OrbCastel E, Masseret E, Laabir M.
553 2016. Toxin and growth responses of the neurotoxic dinoflagellate Vulcanodinium rugosum to
554 varying temperature and salinity. Toxins 8, E136. https://10.3390/toxins8050136.

555 Alonso E, Otero P, Vale C, Alfonso A, Antelo A, Gimenez-Llort L, Chabaud L, Guillou C, Botana
556 LM. 2013. Benefit of 13-desmethyl Spirolide C treatment in triple transgenic mouse model of
557 Alzheimer disease: Beta-Amyloid and neuronal markers improvement. Curr. Alzheimer Res.
558 10, 279-289. https://10.2174/1567205011310030007.

559 Anderson DM, Cembella AD, Hallegraeff GM. 2012. Progress in understanding harmful algal blooms:
560 paradigm shifts and new technologies for research, monitoring, and management. Ann. Rev.
561 Mar. Sci. 4, 143-176. https://10.1146/annurev-marine-120308-081121.

562 Anses. Opinion of the French Agency for Food, Environmental and Occupational Health & Safety on
563 the assessment of the health risks associated with pinnatoxins in shellfish, 2019, pp. 1-23.
564 https://www.anses.fr/en/system/files/ERCA2016SA0013EN.pdf
565 Aráoz R, Barnes P, Sechet V, Delepierre M, Zinn-Justin S, Molgó J, Zakarian A, Hess P, Servent D.
566 2020. Cyclic imine toxins survey in coastal european shellfish samples: Bioaccumulation and
567 mode of action of 28-O-palmitoyl ester of pinnatoxin-G. first report of portimine-A
568 bioaccumulation. Harmful Algae 98, 101887. https://Doi10.1016/j.hal.2020.101887.
569 Aráoz R, Servent D, Molgó J, Iorga BI, Fruchart-Gaillard C, Benoit E, Gu ZH, Stivala C, Zakarian A.
570 2011. Total synthesis of pinnatoxins A and G and revision of the mode of action of pinnatoxin
571 A. J. Am. Chem. Soc. 133, 10499-10511. https://Doi10.1021/Ja201254c.
572 Armit C, Richardson L, Venkataraman S, Graham L, Burton N, Hill B, Yang Y, Baldock RA. 2017.
573 eMouseAtlas: An atlas-based resource for understanding mammalian embryogenesis. Dev.
574 Biol. 423, 1-11. https://10.1016/j.ydbio.2017.01.023.
575 Arnich N, Abadie E, Delcourt N, Fessard V, Fremy JM, Hort V, Lagrange E, Maignien T, Molgó J,
576 Peyrat MB, Vernoux JP, Mattei C. 2020. Health risk assessment related to pinnatoxins in
577 French shellfish. Toxicon 180, 1-10. DOI:10.1016/j.toxicon.2020.03.007.
578 Baddick CG, Marks MJ. 2011. An autoradiographic survey of mouse brain nicotinic acetylcholine
579 receptors defined by null mutants. Biochem. Pharmacol. 82, 828-841.
580 https://10.1016/j.bcp.2011.04.019.
581 Benoit E, Couesnon A, Lindovsky J, Iorga BI, Araoz R, Servent D, Zakarian A, Molgó J. 2019.
582 Synthetic Pinnatoxins A and G Reversibly Block Mouse Skeletal Neuromuscular
583 Transmission In Vivo and In Vitro. Mar. Drugs 17, 306. https://10.3390/md17050306.
584 Bourne Y, Sulzenbacher G, Radic Z, Aráoz R, Reynaud M, Benoit E, Zakarian A, Servent D, Molgó J,
585 Taylor P, Marchot P. 2015. Marine macrocyclic imines, pinnatoxins A and G: Structural
586 determinants and functional properties to distinguish neuronal a7 from Muscle a1(2)bgd
587 nAChRs. Structure 23, 1106-1115. https://doi.org/10.1016/j.str.2015.04.009.
588 Ceccaldi PF, Gavard L, Mandelbrot L, Rey E, Farinotti R, Treluyer JM, Gil S. 2009. Functional role
589 of p-glycoprotein and binding protein effect on the placental transfer of lopinavir/ritonavir in

590 the ex vivo human perfusion model. Obstet. Gynecol. Int. 2009, 726593.
591 https://10.1155/2009/726593.
592 Challier JC. 1985. Criteria for evaluating perfusion experiments and presentation of results. Contrib.
593 Gynecol. Obstet. 13, 32-39. https://doi.org/10.1159/000410667.
594 Couesnon A, Lindovsky J, Zakarian A, Creuzet S, Molgó J. 2014. Pinnatoxins block skeletal
595 neuromuscular junction activity and affect embryo development. Toxicon 91, 175-176.
596 https://10.1016/j.toxicon.2014.08.036.
597 Dauguet J, Delzescaux T, Conde F, Mangin J-F, Ayache N, Hantraye P, Frouin V. 2007. Three-
598 dimensional reconstruction of stained histological slices and 3D non-linear registration with
599 in-vivo MRI for whole baboon brain. J. Neurosci. Methods 164, 191-204.
600 https://doi.org/10.1016/j.jneumeth.2007.04.017.
601 Delcourt N, Lagrange E, Abadie E, Fessard V, Fremy JM, Vernoux JP, Peyrat MB, Maignien T,
602 Arnich N, Molgó J, Mattei C. 2019. Pinnatoxins' Deleterious Effects on Cholinergic
603 Networks: From Experimental Models to Human Health. Mar. Drugs 17, E425.
604 https://10.3390/md17070425.
605 El-Aziz TMA, Ravelet C, Molgó J, Fiore E, Pale S, Amar M, Al-Khoury S, Dejeu J, Fadl M, Ronjat
606 M, Taiwe GS, Servent D, Peyrin E, De Waard M. 2017. Efficient functional neutralization of
607 lethal peptide toxins in vivo by oligonucleotides. Sci. Rep. 7, 7202. https://10.1038/s41598-
608 017-07554-5.
609 Farabegoli F, Blanco L, Rodriguez LP, Vieites JM, Cabado AG. 2018. Phycotoxins in Marine
610 Shellfish: Origin, Occurrence and Effects on Humans. Mar. Drugs 16, 188.
611 https://10.3390/md16060188.
612 Garcia-Altares M, Casanova A, Bane V, Diogene J, Furey A, de la Iglesia P. 2014. Confirmation of
613 pinnatoxins and spirolides in shellfish and passive samplers from Catalonia (Spain) by liquid
614 chromatography coupled with triple quadrupole and high-resolution hybrid tandem mass
615 spectrometry. Mar. Drugs 12, 3706-3732. https://10.3390/md12063706.
616 Gill S, Murphy M, Clausen J, Richard D, Quilliam M, MacKinnon S, LaBlanc P, Mueller R, Pulido O.
617 2003. Neural injury biomarkers of novel shellfish toxins, spirolides: a pilot study using

618 immunochemical and transcriptional analysis. Neurotoxicology 24, 593-604.
619 https://10.1016/S0161-813X(03)00014-7.
620 Griffith AW, Gobler CJ. 2020. Harmful algal blooms: A climate change co-stressor in marine and
621 freshwater ecosystems. Harmful Algae 91, 101590. https://10.1016/j.hal.2019.03.008.
622 Hallegraeff GM. 2010. Ocean climate change, phytoplankton community responses, and harmful algal
623 blooms: A formidable predictive challenge. J. Phycol. 46, 220-235. https://10.1111/j.1529-
624 8817.2010.00815.x.
625 Hellyer SD, Indurthi D, Balle T, Runder-Varga V, Selwood AI, Tyndall JD, Chebib M, Rhodes L,
626 Kerr DS. 2015. Pinnatoxins E, F and G target multiple nicotinic receptor subtypes. J.
627 Neurochem. 135, 479-491. https://10.1111/jnc.13245.
628 Hess P, Abadie E, Herve F, Berteaux T, Sechet V, Aràoz R, Molgó J, Zakarian A, Sibat M,
629 Rundberget T, Miles CO, Amzil Z. 2013. Pinnatoxin G is responsible for atypical toxicity in
630 mussels (Mytilus galloprovincialis) and clams (Venerupis decussata) from Ingril, a French
631 Mediterranean lagoon. Toxicon 75, 16-26. https://doi.org/10.1016/j.toxicon.2013.05.001.
632 Huey R, Hawthorne S, McCarron P. 2017. The potential use of rabies virus glycoprotein-derived
633 peptides to facilitate drug delivery into the central nervous system: a mini review. J. Drug
634 Target 25, 379-385. https://10.1080/1061186X.2016.1223676.
635 Jackson JJ, Stivala CE, Iorga BI, Molgó J, Zakarian A. 2012. Stability of Cyclic Imine Toxins:
636 Interconversion of Pinnatoxin Amino Ketone and Pinnatoxin A in Aqueous Media. J. Org.
637 Chem. 77, 10435-10440. https://Doi10.1021/Jo301632d.
638 Jimenez EC, Olivera BM, Teichert RW. 2007. AlphaC-conotoxin PrXA: a new family of nicotinic
639 acetylcholine receptor antagonists. Biochemistry 46, 8717-8724. https://10.1021/bi700582m.
640 Kvrgić K, Lešić T, Aysal AI, Džafić N, Pleadin J. 2021. Cyclic imines in shellfish and ascidians in
641 the northern Adriatic Sea. Food Addit Contam Part B Surveill 14, 12-22.
642 https://doi.org/10.1080/19393210.2020.1851778.
643 Lamas JP, Arevalo F, Morono A, Correa J, Muniz S, Blanco J. 2019. Detection and spatio-temporal
644 distribution of pinnatoxins in shellfish from the Atlantic and Cantabrian coasts of Spain.
645 Toxins 11, 340. https://10.3390/toxins11060340.

646 Machaalani R, Ghazavi E, Hinton T, Makris A, Hennessy A. 2018. Immunohistochemical expression
647 of the nicotinic acetylcholine receptor (nAChR) subunits in the human placenta, and effects of
648 cigarette smoking and preeclampsia. Placenta 71, 16-23.
649 https://10.1016/j.placenta.2018.09.008.
650 Marks MJ, McClure-Begley TD, Whiteaker P, Salminen O, Brown RWB, Cooper J, Collins AC,
651 Lindstrom JM. 2011. Increased nicotinic acetylcholine receptor protein underlies chronic
652 nicotine-induced up-regulation of nicotinic agonist binding sites in mouse brain. J. Pharmacol.
653 Exp.Ther. 337, 187-200. https://10.1124/jpet.110.178236.
654 McCarron P, Rourke WA, Hardstaff W, Pooley B, Quilliam MA. 2012. Identification of Pinnatoxins
655 and Discovery of Their Fatty Acid Ester Metabolites in Mussels (Mytilus edulis) from Eastern
656 Canada. J. Agric. Food Chem. 60, 1437-1446. https://Doi10.1021/Jf204824s.
657 McCarthy M, Bane V, Garcia-Altares M, van Pelt FN, Furey A, O'Halloran J. 2015. Assessment of
658 emerging biotoxins (pinnatoxin G and spirolides) at Europe's first marine reserve: Lough
659 Hyne. Toxicon 108, 202-9. https://doi.org/10.1016/j.toxicon.2015.10.007.
660 Molgó J, Aráoz R, Iorga BI, Benoit E, Zakarian A. Cyclic imine toxins: chemistry, origin, metabolism,
661 pharmacology, toxicology, and detection. In: Botana LM, editor. Seafood and Freshwater
662 Toxins: Pharmacology, Physiology, and Detection. . CRC Press Inc. Taylor & Francis Inc.,
663 Boca Raton, Florida USA, 2014, pp. 951-989.
664 Molgó J, Marchot P, Araoz R, Benoit E, Iorga BI, Zakarian A, Taylor P, Bourne Y, Servent D. 2017.
665 Cyclic imine toxins from dinoflagellates: a growing family of potent antagonists of the
666 nicotinic acetylcholine receptors. J. Neurochem. 142, 41-51. https://10.1111/jnc.13995.
667 Moreira-González AR, Comas-González A, Valle-Pombrol A, Seisdedo-Losa M, Hernandez-Leyva O,
668 Fernandes LF, Chomérat N, Bilien G, Hervé F, Rovillon GA, Hess P, Alonso-Hernández CM,
669 Mafra LL, Jr., 2021. Summer bloom of Vulcanodinium rugosum in Cienfuegos Bay (Cuba)
670 associated to dermatitis in swimmers. Sci. Total Environ. 757, 143782.
671 https://doi.org/10.1016/j.scitotenv.2020.143782

672 Moreiras G, Leao JM, Gago-Martinez A. 2019. Analysis of Cyclic Imines in Mussels (Mytilus
673 galloprovincialis) from Galicia (NW Spain) by LC-MS/MS. Int J Environ Res Public Health
674 17, 281. https://doi.org/doi:10.3390/ijerph17010281.
675 Munday R, Selwood AI, Rhodes L. 2012. Acute toxicity of pinnatoxins E, F and G to mice. Toxicon
676 60, 995-999. https://10.1016/j.toxicon.2012.07.002.
677 Nézan E, Chomérat N. 2011. Vulcanodinium rugosum gen. Nov., sp. Nov. (dinophyceae): A new
678 marine dinofagellate from French mediterranean coast. Cryptogam. Algol. 32, 3-18.
679 https://DOI:10.7872/crya.v32.iss1.2011.003.
680 Otero P, Miguens N, Rodriguez I, Botana LM. 2019. LC-MS/MS Analysis of the Emerging Toxin
681 Pinnatoxin-G and High Levels of Esterified OA Group Toxins in Galician Commercial
682 Mussels. Toxins (Basel) 11. https://doi.org/10.3390/toxins11070394.
683 Otero P, Vale C, Boente-Juncal A, Costas C, Louzao MC, Botana LM. 2020. Detection of Cyclic
684 Imine Toxins in Dietary Supplements of Green Lipped Mussels (Perna canaliculus) and in
685 Shellfish Mytilus chilensis. Toxins (Basel) 12, 613. https://doi.org/10.3390/toxins12100613.
686 Rambla-Alegre M, Miles CO, de la Iglesia P, Fernandez-Tejedor M, Jacobs S, Sioen I, Verbeke W,
687 Samdal IA, Sandvik M, Barbosa V, Tediosi A, Madorran E, Granby K, Kotterman M, Calis T,
688 Diogene J. 2018. Occurrence of cyclic imines in European commercial seafood and consumers
689 risk assessment. Environ Res 161, 392-398. https://doi.org/10.1016/j.envres.2017.11.028.
690 Rhodes L, Smith FB, Selwood A, McNabb P, Munday R, Suda S, Molenaar S, Hallegraeff G. 2011.
691 Dinoflagellate *Vulcanodinium rugosum* identified as the causative organism of pinnatoxins in
692 Australia, New Zealand and Japan. Phycologia 50, 624-628. https://doi.org/10.2216/11-19.1.
693 Rice D, Barone S, Jr., 2000. Critical periods of vulnerability for the developing nervous system:
694 evidence from humans and animal models. Environ. Health Perspect. 108 Suppl 3, 511-533.
695 https://10.1289/ehp.00108s3511.
696 Rundberget T, Aasen JA, Selwood AI, Miles CO. 2011. Pinnatoxins and spirolides in Norwegian blue
697 mussels and seawater. Toxicon 58, 700-711. https://10.1016/j.toxicon.2011.08.008.

698 Selwood AI, Miles CO, Wilkins AL, van Ginkel R, Munday R, Rise F, McNabb P. 2010. Isolation,
699 Structural Determination and Acute Toxicity of Pinnatoxins E, F and G. J. Agric. Food Chem.
700 58, 6532-6542. https://Doi10.1021/Jf100267a.
701 Selwood AI, Wilkins AL, Munday R, Gu HF, Smith KF, Rhodes LL, Rise F. 2014. Pinnatoxin H: a
702 new pinnatoxin analogue from a South China Sea Vulcanodinium rugosum isolate.
703 Tetrahedron Letters 55, 5508-5510. https://10.1016/j.tetlet.2014.08.056.
704 Sosa S, Pelin M, Cavion F, Herve F, Hess P, Tubaro A. 2020. Acute Oral Toxicity of Pinnatoxin G in
705 Mice. Toxins 12, 87. https://10.3390/toxins12020087.
706 Stivala CE, Benoit E, Aráoz R, Servent D, Novikov A, Molgó J, Zakarian A. 2015. Synthesis and
707 biology of cyclic imine toxins, an emerging class of potent, globally distributed marine toxins.
708 Nat. Prod. Rep. 32, 411-435. https://10.1039/c4np00089g.
709 Sullivan JP, Donnelly-Roberts D, Briggs CA, Anderson DJ, Gopalakrishnan M, Piattoni-Kaplan M,
710 Campbell JE, McKenna DG, Molinari E, Hettinger AM, Garvey DS, Wasicak JT, Holladay
711 MW, Williams M, Arneric SP. 1996. A-85380 [3-(2(S)-azetidinylmethoxy) pyridine]: in vitro
712 pharmacological properties of a novel, high affinity alpha 4 beta 2 nicotinic acetylcholine
713 receptor ligand. Neuropharmacology 35, 725-734. https://doi.org/10.1016/0028-
714 3908(96)84644-2.
715 Van Dolah FM. 2000. Marine algal toxins: origins, health effects, and their increased occurrence.
716 Environ. Health Perspect. 108, 133-141. https://10.1289/ehp.00108s1133.
717 Varriale F, Tartaglione L, Cinti S, Milandri A, Dall'Ara S, Calfapietra A, Dell'Aversano C. 2021.
718 Development of a data dependent acquisition-based approach for the identification of
719 unknown fast-acting toxins and their ester metabolites. Talanta 224, 121842.
720 https://doi.org/10.1016/j.talanta.2020.121842.
721 Ward JM, Cockcroft VB, Lunt GG, Smillie FS, Wonnacott S. 1990. Methyllycaconitine: a selective
722 probe for neuronal alpha-bungarotoxin binding sites. FEBS Lett. 270, 45-48.
723 https://doi.org/10.1016/0014-5793(90)81231-C.

724 Wei X, Zhan C, Shen Q, Fu W, Xie C, Gao J, Peng C, Zheng P, Lu W. 2015. A D-peptide ligand of
725 nicotine acetylcholine receptors for brain-targeted drug delivery. Angew. Chem. Int. Ed. Engl.
726 54, 3023-3027. https://10.1002/anie.201411226.

727

a

PK parameters		
	Mean	SEM
Elimination rate (min^{-1})	0.063	0.015
$T_{1/2}$ (min)	13.1	4.1
T_{max} (min)	2	0
C_{max} (nCi/mL)	539	109
Area Under the Curve (AUC_{0-t}) (min.nCi/mL)	5240	758
Mean Residence Time (MRT_{0-t}) (min)	6.04	0.31
Volume of distribution (mL)	117.4	34.4
Clearance (mL/min)	6.3	0.1

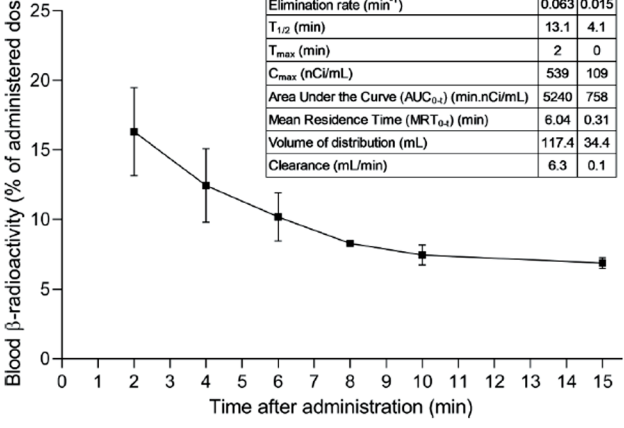

b

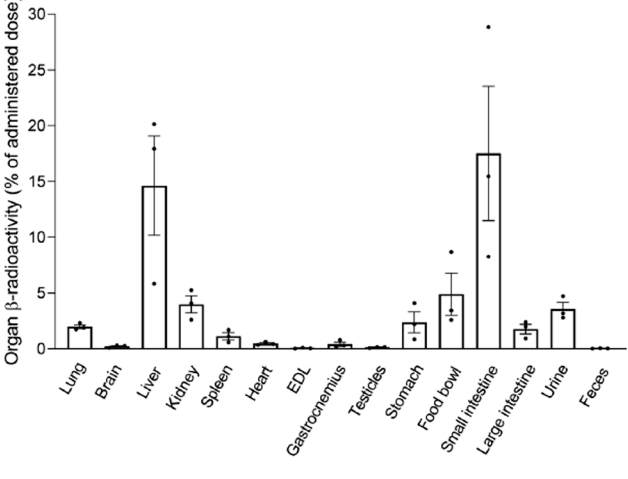

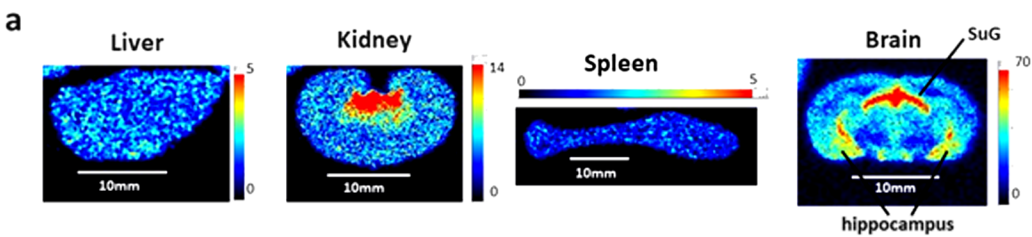
a
Liver
5
0
10mm
Kidney
14
0
10mm
Spleen
0
5
10mm
Brain
SuG
70
0
10mm
hippocampus
b
EDL muscle
6
0
10mm
Gastrocnemius muscle
8
0
10mm
Brain
70
0
10mm

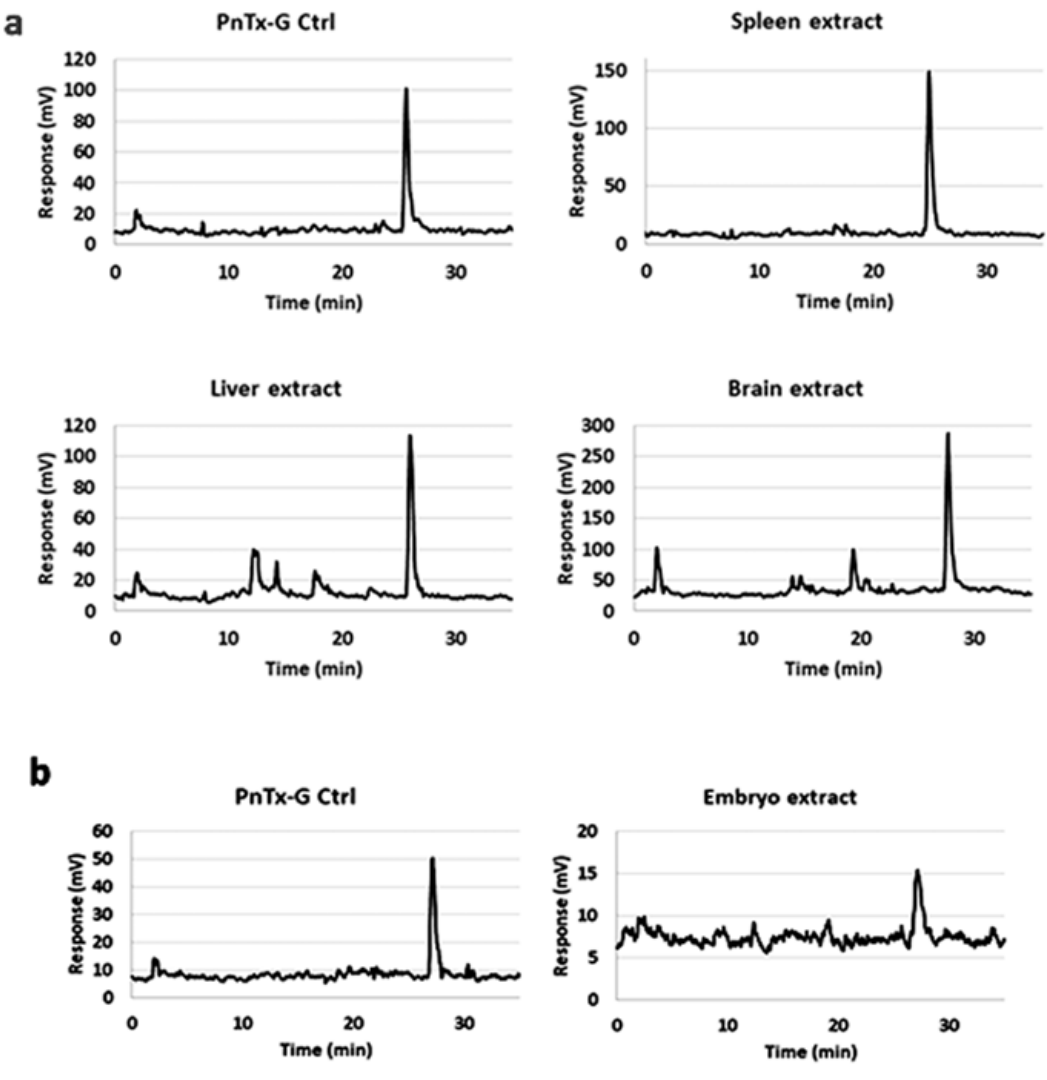
a
PnTx-G Ctrl
Response (mV)
Time (min)
Spleen extract
Liver extract
Brain extract
b
PnTx-G Ctrl
Embryo extract

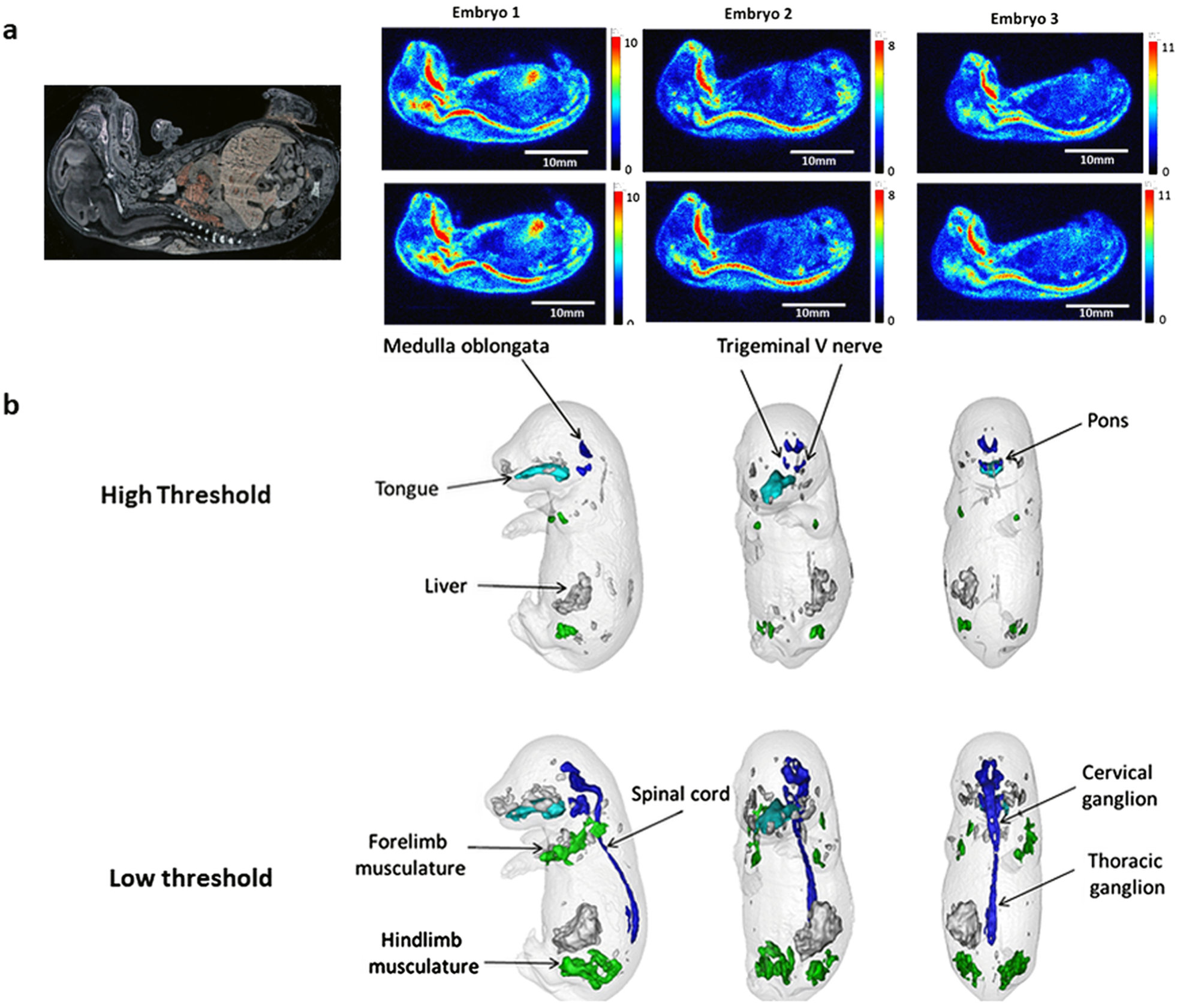
a
Embryo 1
Embryo 2
Embryo 3
10
8
11
0
10mm
b
High Threshold
Low threshold
Medulla oblongata
Trigeminal V nerve
Pons
Tongue
Liver
Spinal cord
Cervical ganglion
Forelimb musculature
Thoracic ganglion
Hindlimb musculature

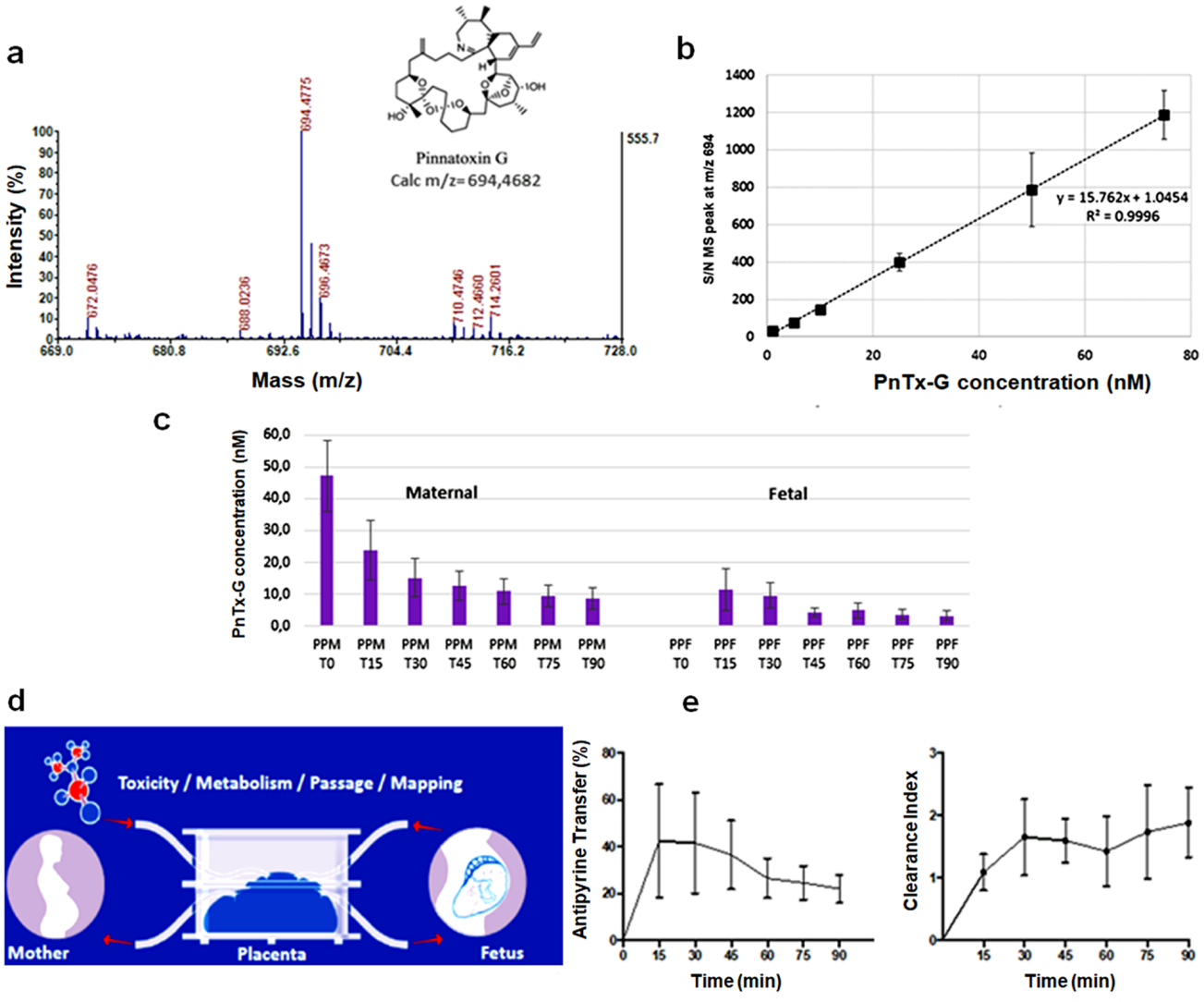
a
Pinnatoxin G
Calc m/z= 694,4682
Intensity (%)
Mass (m/z)
694.4775
555.7
672.0476
688.0236
696.4673
710.4746
712.4660
714.2601
b
S/N MS peak at m/z 694
PnTx-G concentration (nM)
y = 15.762x + 1.0454
R² = 0.9996
c
PnTx-G concentration (nM)
Maternal
Fetal
PPM T0
PPM T15
PPM T30
PPM T45
PPM T60
PPM T75
PPM T90
PPF T0
PPF T15
PPF T30
PPF T45
PPF T60
PPF T75
PPF T90
d
Toxicity / Metabolism / Passage / Mapping
Mother
Placenta
Fetus
e
Antipyrine Transfer (%)
Time (min)
Clearance Index
Time (min)

a

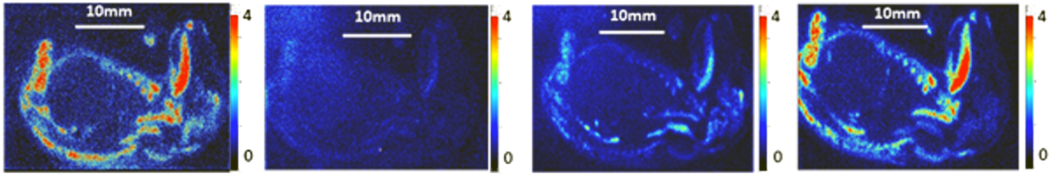

[^{3}H]-PnTx-G (0.3 nM)

[^{3}H]-PnTx-G (0.3 nM)
+ PnTx-G (0.3 μM)

[^{3}H]-PnTx-G (0.3 nM)
+ Conotoxin-PrXA (0.25 μM)

[^{3}H]-PnTx-G (0.3 nM)
+ MLA (100 nM)

b

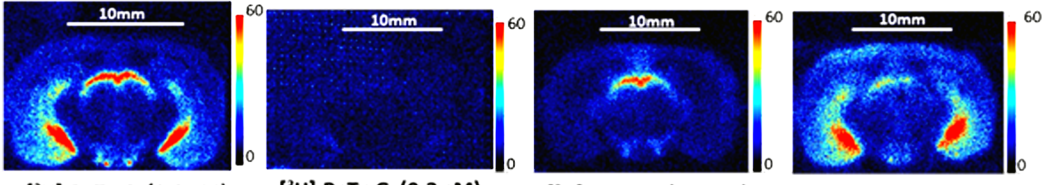

[^{3}H]-PnTx-G (0.3 nM)

[^{3}H]-PnTx-G (0.3 nM)
+ PnTx-G (0.3 μM)

[^{3}H]-PnTx-G (0.3 nM)
+ MLA (100 nM)

[^{3}H]-PnTx-G (0.3 nM)
+ A-85380 (5 nM)

Vulcanodinium rugosum

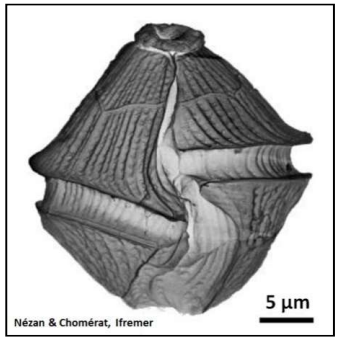

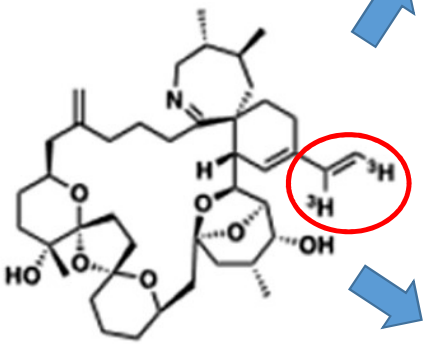

Synthesis, radiolabeling [^{3}H]-Pinnatoxin-G

Oral gavage

Intravenous administration

Cross blood-brain barrier

Rat brain

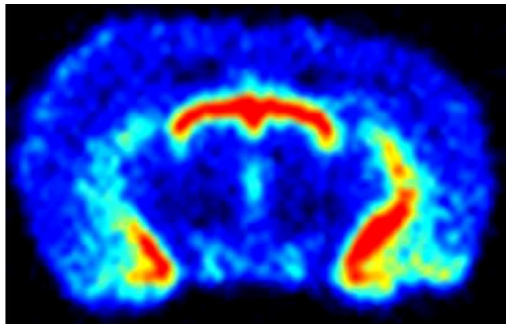

Cross materno-fetal barrier

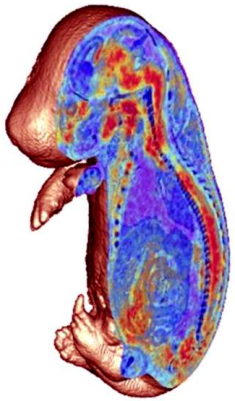

Rat fetus

Human cotyledon